2019

Visualizing Near-Wall Two-Phase Flow Morphology During Confined and Submerged Jet Impingement Boiling to the Point of Critical Heat Flux

C. Mira Hernandez
Purdue University

J. A. Weibel
Purdue University, jaweibel@purdue.edu

S. V. Garimella
University of Vermont, sureshg@purdue.edu

Mira Hernandez, C.; Weibel, J. A.; and Garimella, S. V., "Visualizing Near-Wall Two-Phase Flow Morphology During Confined and Submerged Jet Impingement Boiling to the Point of Critical Heat Flux" (2019). *CTRC Research Publications*. Paper 351.
http://dx.doi.org//10.1016/j.ijheatmasstransfer.2019.07.057

Visualizing near-wall two-phase flow morphology during confined and submerged jet impingement boiling to the point of critical heat flux

Carolina Mira-Hernández, Justin A. Weibel, Suresh V. Garimella
School of Mechanical Engineering, Purdue University
585 Purdue Mall, West Lafayette, IN 47907 USA

Abstract

Confined and submerged two-phase jet impingement is a compact, low-pressure-drop solution for high heat flux dissipation from electronic components. Nucleate boiling can be sustained up to significantly higher heat fluxes during two-phase jet impingement as compared to pool boiling. The increases in critical heat flux are explained via hydrodynamic mechanisms that have been debated in the literature. In this study, the two-phase flow morphology of a single subcooled jet of water that impinges on a circular heat source is visualized at high speed with synchronized top and side views of the confinement gap. The impinging jet issues from a 3.75-mm-diameter orifice that is held at a height of 2 orifice diameters above a 25.4-mm-diameter heat source. The experiments are conducted at a jet Reynolds number of 15,000 and a jet inlet subcooling of 10 °C across a range of heat fluxes up to the critical heat flux. When boiling occurs under subcooled exit flow conditions and at moderate heat fluxes, a regular cycle is observed of formation and collapse of vapor structures that bridge the heated surface and the orifice plate, which causes significant oscillations in the pressure drop. Under saturated exit flow conditions, the vapor agglomerates in the confinement gap into a bowl-like vapor structure that recurrently shrinks, due to vapor break-off at the edge of the orifice plate, and is again replenished due to vapor generation at the heater surface. The optical visualizations from the top of the confinement gap provide a unique perspective and indicate that the liquid jet flows downwards through the vapor structure, impinges on the heated surface, and then flows underneath the vapor structure as a fluid wall jet that wets the heated surface upon which discrete bubbles are generated due to boiling. At high heat fluxes, intense vapor generation causes the fluid wall jet to transition from a bubbly to a churn-like regime, shearing off some liquid droplets into the vapor structure. The origin of critical heat flux appears to result from a significant portion of the liquid in the wall jet being deflected off the surface, and the remaining liquid film on the surface drying out before reaching the edge of the heater.

Keywords

Electronics cooling, jet impingement, nucleate boiling, two-phase flow, flow visualization, critical heat flux.

Nomenclature

Bl^*	modified boiling number, $(\pi / 4) D^2 q'' \big/ \dot{m} c_p \left(T_{sat} - T_j\right)$
c_p	fluid specific heat
d	orifice diameter
D	heat source diameter
H	confinement gap height
l	orifice plate thickness
$\dot{m}$	mass flow rate
p_{op}	operating pressure
q''	heat flux
Re	Reynolds number, $\left(\rho_j v_j d / \mu_j\right)$
t	time
T_s	surface temperature
T_{sat}	saturation temperature
ΔT_{sub}	degree of subcooling (T_{sat} - T_j)
v	velocity

Greek symbols

μ	fluid dynamic viscosity
ρ	fluid density

Subscript

j	jet inlet condition
s	surface
sat	saturated condition

1. Introduction

Two-phase jet impingement is an attractive cooling technology that allows dissipation of high heat fluxes at low wall superheats [1–4]. During two-phase jet impingement, the mode of heat transfer depends on the surface heat flux. At low heat fluxes, single-phase heat transfer exists over the entire surface; the heat transfer coefficient is non-uniform across the surface, with a peak at the stagnation point directly under the jet orifice and lower values in the wall jet region approaching the periphery of the heated surface. As the heat flux increases, nucleate boiling initiates at the periphery of the surface, and creeps inwards toward the stagnation region [5–8]. Further increases in heat flux cause nucleate boiling to occur over the entire heated surface and a fully boiling regime is achieved. During fully boiling, the heat transfer coefficient across the surface is relatively uniform and insensitive to conditions of the liquid jet, such as velocity and subcooling [1,2,9–11]. Based on these observed heat transfer modes, Mira-Hernández *et al.* [12] developed and validated a semi-empirical model for predicting two-phase heat transfer from arrays of confined and submerged impinging jets.

A key difference between boiling in a stagnant pool and fully boiling during jet impingement is that the inclusion of the jet significantly delays the occurrence of critical heat flux, which enables operation in the efficient nucleate boiling regime up to higher heat fluxes [1,2,9,11,13,14]. This phenomenon was reported by Katto and Kunihiro [9] while evaluating two alternatives to extend the nucleate boiling from a horizontal surface in a shallow pool of water, namely, forced collapse of the vapor structures by mechanical means, and liquid supply to the surface by a saturated impinging jet. Improvements to critical heat flux using forced bubble collapse were limited by bubble dynamics. Much larger increases in critical heat flux were obtained using the saturated impinging jet. The authors suggested that the critical heat flux in the presence of the impinging jet occurred when the liquid supply to the heated surface was hindered by splashing of the jet due to vapor generation at the surface.

A mechanistic understanding of critical heat flux during two-phase jet impingement is still lacking. Several studies have experimentally measured the critical heat flux in free surface jets and developed empirical correlations [1,2,13,15–19]. The functional form of the empirical correlations has been determined either from dimensional analysis or by considering possible mechanisms that can trigger critical heat flux [1]. Lienhard and Eichhorn [15] applied a mechanical energy stability criterion to the case of a free surface jet impinging on a flat surface, and postulated that critical heat flux occurs when the kinetic energy of the upward vapor flow exceeds the energy expended in the formation of droplets that shear away from the heated surface. Monde [16] proposed a different mechanism for critical heat flux for a free surface impinging jet, which postulated that the jet supplies liquid to the heated surface via a thin liquid layer that exists underneath large vapor bubbles. The vapor generated at the surface flows upwards across the thin liquid layer in the form of discrete vapor columns into the large vapor bubbles. The critical

heat flux condition is reached when the liquid film fed by the jet dries out. In both studies [15,16], the critical heat flux is found to be proportional to the cube root of the jet velocity. This functional dependency has been confirmed in several experimental studies for free-surface jets under moderate velocities and near atmospheric pressures [1,2]. Other functional dependencies have been identified under less common operating conditions, such as at very low or very high jet velocities and near critical pressures [17,19].

For confined, submerged two-phase jet impingement, fewer parametric studies of the critical heat flux phenomenon have been performed despite the suitability of this configuration for compact electronics cooling. Mudawar and Wadsworth [13] performed an experimental study on critical heat flux for planar confined jets of FC-72 and developed an empirical correlation for moderate jet velocities that predicts a considerably stronger dependence on jet velocity ($q''_{CHF} \sim v_j^{0.7}$) than in the case of free-surface jets ($q''_{CHF} \sim v_j^{0.33}$); this was attributed to flow confinement effects that prevent the bulk flow of liquid from separating from the heated surface [13]. For high jet velocities, a reduction in the critical heat flux with increase in velocity was observed, which was attributed to entrapment of vapor bubbles that have insufficient momentum to enter the bulk flow. In experiments with HFE-7100 at moderate velocities, Clark *et al.* [11] also found a strong dependence of critical heat flux on jet velocity with an almost linear relationship.

During confined, submerged two-phase jet impingement of water at low orifice-to-target spacings, the formation of large vapor structures in the confinement gap has been observed for a wide range of surface heat fluxes [20]. The vapor structures remain in the confinement gap for long periods as compared with the characteristic times for formation and departure of large vapor bubbles during nucleate pool boiling. However, the heat transfer performance does not deteriorate, and the nucleate boiling regime is still significantly extended beyond the critical heat flux for pool boiling. This behavior is intriguing because it indicates that, for this configuration, the main effect of the jet is not to remove vapor from the confinement gap but to continuously rewet the surface by breaking through the vapor structure close to the heated surface. The current study investigates the connection between the flow morphology inside the confinement gap and the extension of the nucleate boiling regime during two-phase jet impingement of water at small orifice-to-target spacings. For characterization of the flow morphology, synchronized high-speed visualizations are performed from the top and the side of the confinement gap. During confined and submerged jet impingement, two-phase flow morphology characterization has been mainly limited to optical visualizations from the side of the confinement gap [11,20–22], but the formation of large vapor structures prevents examination of flow phenomena close to the surface in the side view. Visualization from the top of the confinement gap, as performed in this work, enables direct observation of boiling

behavior on the heated surface, which is critical to unraveling the connection between flow morphology and the occurrence of critical heat flux.

2. Experimental methods

2.1. Flow loop

Figure 1 a shows a diagram of the flow loop that is used to perform the experiments and is described in detail in Ref. [21]. The flow loop delivers degassed water to the test section at a controlled mass flow rate and temperature. Water is circulated through the loop by a magnetically-coupled gear pump with adjustable rotational speed. The mass flow rate to the test section is measured by a Coriolis flow meter (CMFS015M, Emerson), and finely tuned by controlling the flow through a bypass loop with a metering valve. The power input to a preheater upstream of the test section is adjusted to set the inlet temperature. Water is drawn from and returns to a reservoir that is open to the ambient. The liquid in the reservoir is continuously boiled during testing to maintain a degassed state, and the reservoir is hence at the saturation temperature. The water is slightly cooled in a heat exchanger downstream of the reservoir to prevent cavitation in the pump.

2.2. Test section

Figure 1b presents a schematic illustration of the test section, in which the plenum is modified from the original design in Ref. [21] to permit visualization of the flow from the top of the confinement gap. The walls of the test section are made of polyether ether ketone (PEEK), except for the front and back walls, which are made of polycarbonate to allow side-view optical access of the confinement gap. Liquid enters laterally at the top of the plenum through a radial flow distributor as shown in Figure 1c. The radial flow distributor attenuates the turbulence and asymmetry in the flow induced by the lateral fluid inlet and is additively manufactured using polyamide 12 (PA 12) [23]. Inside the radial flow distributor, a baffle diverts the liquid to flow circumferentially along an annular channel. From there, the liquid flows radially through slits in the inner wall of the annular channel and into the plenum. The liquid then flows downward in the straight section of the polycarbonate plenum of inner diameter 69.85 mm and length 113 mm, before entering a sharp-edged orifice at the bottom of the plenum to form an impinging liquid jet. The jet orifice has a diameter of 3.75 mm and a length of 6.35 mm. A T-type thermocouple is inserted through a port in the radial flow distributor and bent downward to measure the liquid temperature just upstream of where the jet is formed. A capillary tube is similarly inserted to probe the pressure upstream of the orifice. The pressure probe is connected to a differential pressure transducer (Omega PX409-015DWU5V-EH) to measure the difference in pressure upstream of the orifice and inside the chamber. The orifice plate, as well as the plate that seals the plenum on the top, are transparent and made

of polycarbonate. The jet flows into a confinement gap of height 7.50 mm (H/d = 2) and diameter 76.20 mm.

The jet impinges on a smooth circular heated surface of 25.4 mm diameter that is gold-plated to prevent oxidation. The heated surface is the top of a copper block composed of two cylindrical sections. The lower section of the copper block has a larger diameter to accommodate twelve 100 W cartridge heaters. Along the top section of the copper block, rakes of T-type thermocouples (± 0.5 K) are positioned to provide the surface temperature by extrapolation, assuming a linear profile. The uncertainty in the extrapolated surface temperature is approximately 1.3 ºC at the lowest heat flux and 1.8 ºC at the highest heat flux. The copper block is sealed flush to the bottom wall of the test section with a small bead of silicone sealant, and circumferentially insulated with ceramic fiber. A heat loss analysis is performed using a numerical model to estimate the actual heat flux into the fluid, as described in Ref. [24]. The uncertainty in heat flux is less than 2 %, and includes contributions from uncertainty in surface temperature and electric power input. After impingement, the fluid flows beyond the confinement gap and leaves the chamber through an exit port on the top wall. The absolute pressure inside the chamber is monitored with a pressure tap (Gems 2200BG3F002A3UA) located at the bottom of the test section. The bath temperature is measured by a T-type thermocouple that is inserted through the side wall of the test section.

2.3. Experimental procedure

Before running the two-phase jet impingement experiments, the flow loop and the test section are filled with water and a degassing procedure is initiated. During degassing, the fluid is circulated through the flow loop at 480 ml/min, and any solid contaminants larger than 7 μm are trapped in the particulate filter. Immersion heaters are used to vigorously boil the water in the reservoir, while the power to the preheater is adjusted to keep the temperature in the test section at ~80 °C. The vapor generated in the reservoir is condensed in two Graham reflux condensers located on the top of the reservoir, while non-condensable gases are vented. Surface aging has been commonly observed in boiling experiments, and in some cases, surface priming procedures have been implemented [25]. After degassing for 6 h, a priming procedure is performed on the heated surface to attenuate the effect of surface aging on the consistency of the boiling behavior. For surface priming, the flow rate is increased to ~1100 ml/min, the particulate filter is bypassed, and the power input to the cartridge heaters inside the copper block is set to a relatively high value of around 700 W. After obtaining a steady response, the flow rate and inlet temperature are gently adjusted to the experimental conditions – a flow rate of 860 ml/min and an inlet temperature of 90 °C – and the surface is allowed to boil for an extended period to prime the surface. When consistent boiling behavior is achieved, the power to the heated surface is turned off and the experiment is started.

During the jet impingement experiments, power to the heated surface is increased in steps starting from 100 W until the critical heat flux is reached, as characterized by a dramatic rise in the surface temperature after a power increment. The power is kept constant at each increment until the system reaches a steady state. If necessary, the flow rate and inlet temperature are finely readjusted at each increment to maintain the nominal experimental conditions, namely, a Reynolds number of 15000 and an inlet subcooling of 10 °C. At steady state, temperature and flow data are acquired at 0.5 Hz and recorded for 2 min. During steady-state operation, synchronized high-speed videos of the flow in the confinement gap are acquired through the top of the plenum (Phantom Veo 710L) and the side of the test section (Phantom v1212) at 2000 fps each. A separate data acquisition system is used to record pressure drop data at high frequency; these measurements are also synchronized with the high-speed visualizations. Across the range of tested heat fluxes, the mean pressure drop remains nearly constant at 1.2 kPa with a standard deviation in the mean pressure drop of 0.03 kPa.

3. Results and discussion

The boiling curve obtained during the jet impingement experiments is presented in Figure 2. The boiling curve includes all characteristics expected of the heat transfer modes that occur during jet impingement: single-phase heat transfer with a linear relationship between heat flux and wall superheat ($q'' < 35$ W/cm^2), partial boiling heat transfer as a transition mode, and fully boiling heat transfer with a weak non-linear dependence on the heat flux of the wall superheat ($q'' > 144$ W/cm^2). The boiling curve extends up to a heat flux of 255 W/cm^2, which is the last steady-state operating point that was tested before the next power increment induced critical heat flux. This maximum heat flux is ~2.3 times the value of critical heat flux predicted by Zuber's correlation [26] for pool boiling of 110 W/cm^2, which is a standard benchmark in boiling studies.

The morphology of vapor structures inside the confinement gap is controlled by the balance between vapor generation due to boiling at the heated surface and vapor condensation in the confinement gap due to the jet subcooling. The modified boiling number, $Bl^* = (\pi / 4) D^2 q'' \big/ \dot{m} c_p \left(T_{sat} - T_j\right)$, introduced by Rau *et al.* [20], is a heat flux non-dimensionalization that is used to characterize the thermodynamic state of the fluid at the exit as either subcooled, $Bl^* < 1$, or saturated, $Bl^* \geq 1$. Relative to use of a vapor quality, the modified boiling number is more useful in describing the phenomena of interest that span across subcooled and saturated exit flow conditions. The flow morphologies observed during the jet impingement experiments are classified according to the thermodynamic exit condition of the fluid, namely, as having subcooled or saturated exit flow conditions, and are described in detail in the following.

3.1. Flow morphology during subcooled exit flow conditions

During subcooled exit flow conditions, the vapor generated due to boiling at the heater condenses inside the confinement gap, and the morphology of vapor structures inside the gap strongly depends on the heat flux, which controls the rate of vapor generation. Figure 3a and Figure 3b respectively present the top- and side-view observations of the flow morphology during these subcooled exit flow conditions (supplementary videos are available in the Appendix). Figure 3c displays a time-averaged intensity map that indicates the percentage of time that vapor is present at each location in the side-view images of the confinement gap. Figure 3d shows sketches of the flow morphology based on the visualizations. The map of time-averaged vapor presence is constructed from masks for the vapor phase in individual side-view frames. An image-processing algorithm is applied to the grayscale images to segment the vapor phase. The masking algorithm takes advantage of the dynamic nature of the flow morphology, and identifies the vapor phase as the pixels that poorly correlate between frames. To attenuate the effects of non-uniform illumination, a standard deviation filter is applied before estimating the correlation between image frames.

At $Bl^* \sim 0.4$, nucleate boiling starts. Inside the fluid wall jet, nucleation and growth of tiny bubbles is observed, with a higher concentration at the periphery of the heated surface where the single-phase heat transfer coefficient is the lowest (Figure 3a). The tiny bubbles either condense inside the jet stream or are dragged to the edge of the heat source, and do not escape from the wall jet into the confinement gap. The bubbles coalesce as they are dragged to the periphery to form small vapor petals around the edge of the circular heated surface. Continuous vapor condensation prevents the petals from growing and departing the heated surface into the confinement gap as discrete vapor bubbles and vapor is only present in the vicinity of the heat source (Figure 3c). A few air bubbles at the top of the confinement gap (underside of the orifice plate) slightly occlude the top view, despite extensive degassing.

Increases in heat flux intensify the vapor generation ($Bl^* \sim 0.62$), and the rim of petals is able to grow into bubbles that depart from the surface and condense inside the confinement gap. When $Bl^* \sim 0.78$, the vapor is generated fast enough that the petals grow into vapor blobs that partially bridge the confinement gap, without departing from the heated surface. The blobs merge into a single vapor structure. Then, the vapor structure collapses due to condensation and the blobs start forming again. The growing blobs are noticeable in the top view in Figure 3a. The bubble in the center of the image is an air bubble that is attached to the orifice plate. Two different images of the vapor flow morphology are included in the side-view observations in Figure 3b at $Bl^* \sim 0.78$ to illustrate the two key states, formation (state 1) and growth (state 2) of the vapor blobs. To represent the transient alternation between these states, they are respectively drawn in dark versus light gray in the flow morphology sketches in Figure 3d. On average, the vapor spans the height of the confinement gap but does not escape the confinement gap (Figure 3c).

When the exit flow is close to saturation, $Bl^* = 0.94$, vapor generation is strong enough to form an unsteady, bowl-like axisymmetric vapor structure that bridges across the confinement gap and expands toward the outer edge of the orifice plate. In some instances, the bowl-like structure breaks into a vapor layer at the top of the confinement gap and a thick vapor rim attached to the heat source (Figure 3b, state 1). The bowl-like vapor structure is reformed as the vapor rims grows and reconnects with the top vapor layer (Figure 3b, state 2). In other instances, the bowl-like vapor structure extends beyond the edge of the orifice plate and some vapor escapes the confinement gap; afterward, the vapor structure either shrinks or breaks into two parts.

When the bowl-like vapor structure forms, the heated surface can be seen through the vapor in the top view, Figure 3a ($Bl^* = 0.94$). However, this view can be obstructed by liquid droplets that condense on the underside of the relatively colder orifice plate. The condensed droplets are swept away when the vapor structure breaks due to condensation, or when it shrinks due to vapor escaping from the gap, which enables unobstructed visualization of the boiling phenomena at the surface at some intervals. Although bubble nucleation occurs on the entire surface for $Bl^* = 0.94$, the density increases with the distance from the center of the heater, and nucleation sites are sparse in the vicinity of the impingement region under the orifice.

The dynamic behavior of the vapor structures in the confinement gap causes oscillations in the pressure drop between the inlet plenum and downstream of the confinement gap, with a magnitude that is linked to the vapor morphology. Figure 4 presents the relative standard deviation in pressure drop for the tested heat fluxes along with schematic illustrations of the observed vapor morphology inside the confinement gap. Slight oscillations occur during single-phase heat transfer and boiling at low heat fluxes ($Bl^* < 0.62$). When the vapor blobs grow large enough to form vapor bridges in the confinement gap, the amplitude of pressure oscillations increases due to partial obstruction of the jet flow. The amplitude of oscillations reaches a maximum when the exit flow is close to saturation ($Bl^* = 0.94$) and the vapor morphology is an unsteady bowl-like structure.

3.2. Flow morphology during saturated exit flow conditions

Figure 5 presents the observed flow morphology during saturated exit flow conditions (supplementary videos of top- and side-view visualizations are available in the Appendix). When the boiling number is increased above unity, vapor escapes the confinement gap frequently by breaking off when the bowl-like vapor structure reaches the edge of the orifice plate. The vapor structure alternates between a reestablishing vapor bowl, and an asymmetric shape skewed at the top towards one side of the orifice plate where the vapor breaks off. The shape evolution of the vapor structure is best observed in the videos available in the Appendix. As seen in Figure 4, the amplitude of the oscillations in pressure decreases dramatically when the exit flow thermodynamic conditions become saturated, and vapor

continuously bridges the confinement gap (Figure 5c). From this point on, the amplitude of pressure oscillations increases almost monotonically with heat flux (Figure 4) because the vapor break-off events become more frequent and dramatic. At high heat fluxes, $Bl^* > 1.78$, as the vapor bowl is reestablished, the confinement gap can be completely covered with vapor, and the vapor break-off can be violent enough to almost clear all vapor from the gap.

Top view observations indicate that the liquid jet flows downward through the vapor structure and impinges on the surface. The heated surface is always visible through the orifice across the tested heat fluxes, which confirms that the jet is not diverted by the vapor before it impinges (see Figure 3a and Figure 5a). After impingement, the liquid jet transforms into a fluid wall jet, flowing radially outwards underneath the vapor structure. Boiling occurs within the fluid wall jet, exhibiting different flow regimes that depend on the heat flux. Under saturated exit flow conditions and up to a heat flux of ~175 W/cm^2, $1.0 > Bl^* > 1.44$, intense boiling occurs on the entire heated surface in a bubbly flow regime, as can be seen in the top view in Figure 5a, and is illustrated in the corresponding sketch of the flow morphology in Figure 5d. The vapor bubbles accumulate into the vapor structure and ultimately escape the confinement gap at the top, while the remaining liquid is expelled at the edge of the heated surface. This provides direct evidence that the impinging jet extends the nucleate boiling regime by a mechanism of continuously wetting the heated surface.

As the heat flux is increased further, the intense vapor generation at the surface significantly disrupts the flow of the fluid wall jet. As can be seen in Figure 5a, for the heat flux of 215 W/cm^2 and $Bl^* = 1.78$, the fluid wall jet flow becomes more chaotic with increasing radius, signaling a churn-like behavior. Also part of the fluid wall jet is sheared off the surface, and some liquid droplets break into the vapor structure. The portion of the liquid flow that remains attached to the surface forms a liquid film that extends to the edge of the heater. Figure 6a presents a detailed view of the characteristic flow morphology at high heat fluxes, with a magnified top-view image next to a schematic illustration that shows the transition from bubbly to churn-like flow in the fluid wall jet and the presence of sheared liquid droplets. Close examination of the high-speed videos indicates that the sheared droplets travel inside the vapor structure to the liquid-vapor interface and merge with the liquid in the bath. Figure 6b details the flow path of a single sheared droplet with a set of time-sequence image frames.

At the last steady-state operating point before critical heat flux, $q'' = 255$ W/cm^2 and $Bl^* = 2.11$, bubbly flow is almost absent in the wall jet in the top view visualizations. Churn-like flow dominates the fluid wall jet except in the impinging region, where discrete tiny bubbles can still be recognized. The splashing of the liquid film due to shearing is very strong, and the liquid-vapor interface is heavily disrupted. At this operating point very close to the critical heat flux, transient spikes are observed in the surface temperature signals, which suggest partial dryout of the heated surface. These flow morphology

observations, particularly visualizations from the top of the confinement gap, indicate that critical heat flux occurs when a significant portion of the liquid in the wall jet is diverted away from the surface due to splashing and the remaining liquid film that flows attached to the heater surface dries out before reaching the edge.

4. Conclusion

Experiments are conducted with a single, confined and submerged water jet undergoing boiling after impinging on a circular heated surface to investigate the coupling between two-phase flow morphology and the extension of the nucleate boiling regime. The flow morphology is characterized across a range of heat fluxes that includes subcooled and saturated exit flow conditions, from incipience to critical heat flux. Under subcooled exit flow conditions, the morphology of vapor structures strongly depends on the heat flux, which controls the vapor generation rate. Frequent collapse of the vapor structures due to condensation induces strong oscillations in the pressure drop. When saturated exit flow conditions are reached at higher heat fluxes, a characteristic dynamic behavior of the vapor structure inside the confinement gap is established. The vapor agglomerates inside the gap into a bowl-like shape that continuously grows due to vapor generation and momentarily shrinks when vapor breaks off at the edge of the orifice plate.

First-of-their-kind flow visualizations from the top of the confinement gap allow us to conclude that the liquid jet flows downward through the vapor structure, impinges on the surface, and then flows underneath the vapor structure as a fluid wall jet; bubbles nucleate at the heated surface and grow inside this fluid wall jet. These observations confirm that continual surface rewetting is the mechanism by which the liquid jet extends the nucleate boiling regime beyond the critical heat flux limit encountered in pool boiling. At high heat fluxes, the fluid wall jet becomes more chaotic with increasing radius, indicating a transition from a bubbly to a churn-like flow regime. Also, shearing of liquid droplets from the fluid wall jet into the bowl-like vapor structure is observed. At the highest heat flux before critical heat flux, a churn-like flow regime is dominant and significant shearing of liquid droplets occurs. These observations indicate that critical heat flux occurs because the intense vapor generation diverts a considerable portion of the liquid in the wall jet away from the heater, and the remaining portion that is able to wet the surface dries out before reaching the edge.

Acknowledgements

Carolina Mira-Hernández acknowledges financial support from the Colombia-Purdue Institute (CPI) and the Colombian department for science, technology and innovation (Colciencias). The authors thank Dr. Pavlos P. Vlachos for his feedback on the plenum design for top-view visualization, Matthew D. Clark for

his input regarding the modifications to the experimental setup, and Casey Carter for her assistance during data collection.

Appendix

Supplementary data associated with this article can be found in the online version.

References

[1] D. H. Wolf, F. P. Incropera, and R. Viskanta, "Jet impingement boiling," *Adv. Heat Transf.*, vol. 23, pp. 1–132, 1993.

[2] L. Qiu, S. Dubey, F. H. Choo, and F. Duan, "Recent developments of jet impingement nucleate boiling," *Int. J. Heat Mass Transf.*, vol. 89, pp. 42–58, 2015.

[3] C. F. Ma, Y. P. Gan, and D. H. Lei, "Liquid jet impingement heat transfer with or without boiling," *J. Therm. Sci.*, vol. 2, no. 1, pp. 32–49, 1993.

[4] I. Mudawar, "Assessment of high-heat-flux thermal management schemes," *IEEE Trans. Components Packag. Technol.*, vol. 24, no. 2, pp. 122–141, 2001.

[5] M. J. Rau, E. M. Dede, and S. V. Garimella, "Local single- and two-phase heat transfer from an impinging cross-shaped jet," *Int. J. Heat Mass Transf.*, vol. 79, pp. 432–436, 2014.

[6] D. T. Vader, F. P. Incropera, and R. Viskanta, "Convective nucleate boiling on a heated surface cooled by an impinging, planar jet of water," *J. Heat Transfer*, vol. 114, no. 1, pp. 152–160, 1992.

[7] D. H. Wolf, F. P. Incropera, and R. Viskanta, "Local jet impingement boiling heat transfer," *Int. J. Heat Mass Transf.*, vol. 39, no. 7, pp. 1395–1406, 1996.

[8] N. M. Dukle and D. K. Hollingsworth, "Liquid crystal images of the transition from jet impingement convection to nucleate boiling part II: Nonmonotonic distribution of the convection coefficient," *Exp. Therm. Fluid Sci.*, vol. 12, no. 3, pp. 288–297, Apr. 1996.

[9] Y. Katto and M. Kunihiro, "Study of the mechanism of burn-out in boiling system of high burn-out heat flux," *Bull. JSME*, vol. 16, no. 99, pp. 1357–1366, 1973.

[10] C. F. Ma and A. E. Bergles, "Boiling jet impingement cooling of simulated microelectronic chips," *Heat Transf. Electron. Equip.*, vol. 1, pp. 5–12, 1983.

[11] M. D. Clark, J. A. Weibel, and S. V. Garimella, "Identification of nucleate boiling as the dominant heat transfer mechanism during confined two-phase jet impingement," *Int. J. Heat Mass Transf.*, vol. 128, pp. 1095–1101, 2019.

[12] C. Mira-Hernández, M. D. Clark, J. A. Weibel, and S. V. Garimella, "Development and validation of a semi-empirical model for two-phase heat transfer from arrays of impinging jets," *Int. J. Heat Mass Transf.*, vol. 124, pp. 782–793, 2018.

[13] I. Mudawar and D. C. Wadsworth, "Critical heat flux from a simulated chip to a confined rectangular impinging jet of dielectric liquid," *Int. J. Heat Mass Transf.*, vol. 34, no. 6, pp. 1465–1479, 1991.

[14] R. Cardenas and V. Narayanan, "Heat transfer characteristics of submerged jet impingement boiling of saturated FC-72," *Int. J. Heat Mass Transf.*, vol. 55, no. 15–16, pp. 4217–4231, 2012.

[15] J. H. Lienhard and R. Eichhorn, "On predicting boiling burnout for heaters cooled by liquid jets," *Int. J. Heat Mass Transf.*, vol. 22, no. 5, pp. 774–776, 1979.

[16] M. Monde, "Critical heat flux in saturated forced convective boiling on a heated disk with and impinging jet," *Wärme - und Stoffübertragung*, vol. 19, pp. 205–209, 1985.

[17] M. Monde and T. Inoue, "Critical heat flux in saturated forced convective boiling on a heated disk with multiple impinging jets," *J. Heat Transfer*, vol. 113, no. 3, p. 722, 1991.

[18] M. Kandula, "Mechanisms and predictions of burnout in flow boiling over heated surfaces with an impinging jet," *Int. J. Heat Mass Transf.*, vol. 33, no. 9, pp. 1795–1803, 1990.

[19] Y. Katto and M. Shimizu, "Upper limit of CHF in the saturated forced convection boiling on a heated disk with a small impinging jet," *J. Heat Transfer*, vol. 101, no. 2, p. 265, 1979.

[20] M. J. Rau, P. P. Vlachos, and S. V. Garimella, "A tomographic-PIV investigation of vapor-induced flow structures in confined jet impingement boiling," *Int. J. Multiph. Flow*, vol. 84, pp. 86–97, 2016.

[21] M. J. Rau, T. Guo, P. P. Vlachos, and S. V. Garimella, "Stereo-PIV measurements of vapor-induced flow modifications in confined jet impingement boiling," *Int. J. Multiph. Flow*, vol. 84, pp. 19–33, 2016.

[22] C. H. Shin, K. M. Kim, S. H. Lim, and H. H. Cho, "Influences of nozzle-plate spacing on boiling

heat transfer of confined planar dielectric liquid impinging jet," *Int. J. Heat Mass Transf.*, vol. 52, no. 23–24, pp. 5293–5301, 2009.
[23] HP Development Company, "HP 3D High Reusability PA 12," Palo Alto, CA, 2017.
[24] M. J. Rau and S. V. Garimella, "Confined jet impingement with boiling on a variety of enhanced surfaces," *J. Heat Transfer*, vol. 136, no. 10, p. 101503, 2014.
[25] S. M. You, A. Bar-Cohen, and T. W. Simon, "Boiling incipience and nucleate boiling heat transfer of highly wetting dielectric fluids from electronic materials," *IEEE Trans. Components, Hybrids, Manuf. Technol.*, vol. 13, no. 4, pp. 1032–1039, 1990.
[26] N. Zuber, "On the stability of boiling heat transfer," *Trans. ASME*, vol. 80, 1958.

List of figures

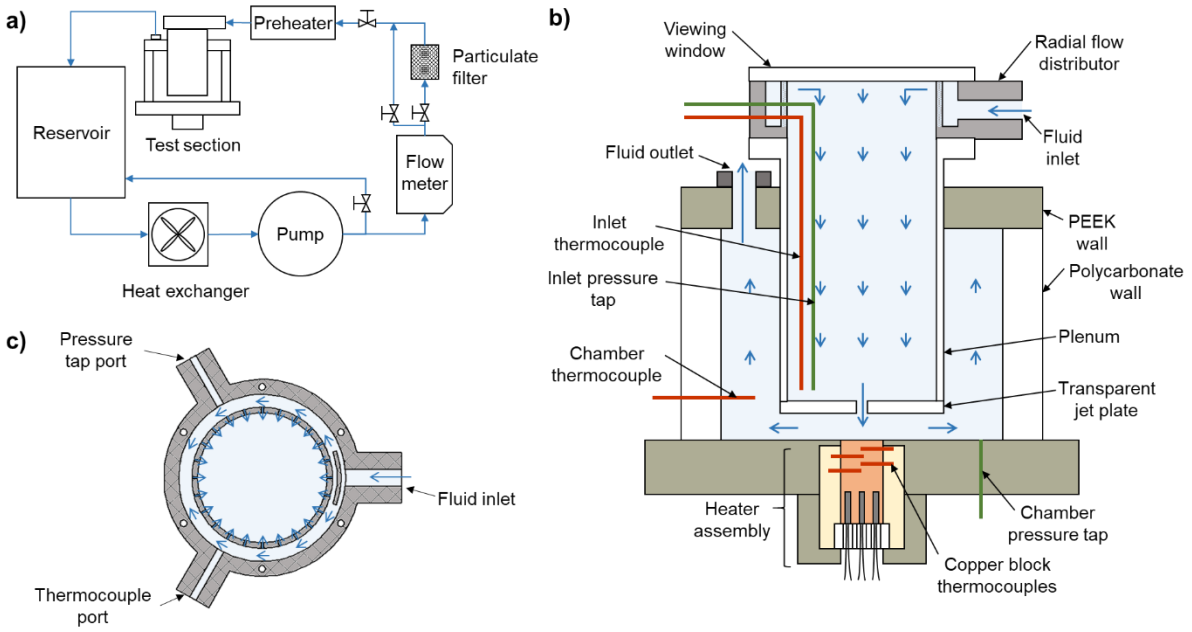

Figure 1. (a) Flow loop diagram, (b) schematic illustration of the test section, and (c) cross-sectional top view of the radial flow distributor.

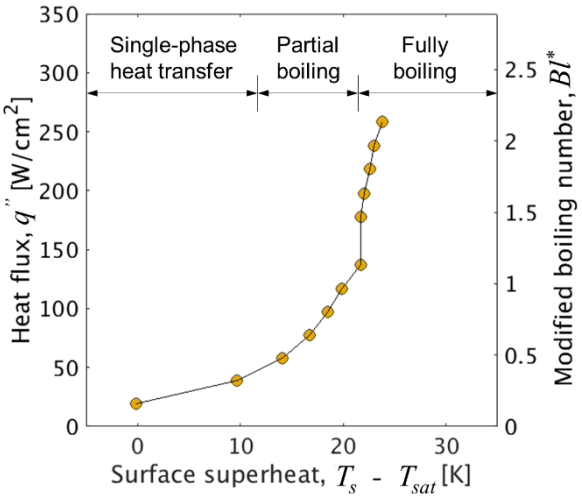

Figure 2. Boiling curve during two-phase jet impingement of a water jet on a circular heater (d = 3.75 mm, Re = 15000, H/d = 2, ΔT_{sub} = 10 K, p_{op} = 1 atm).

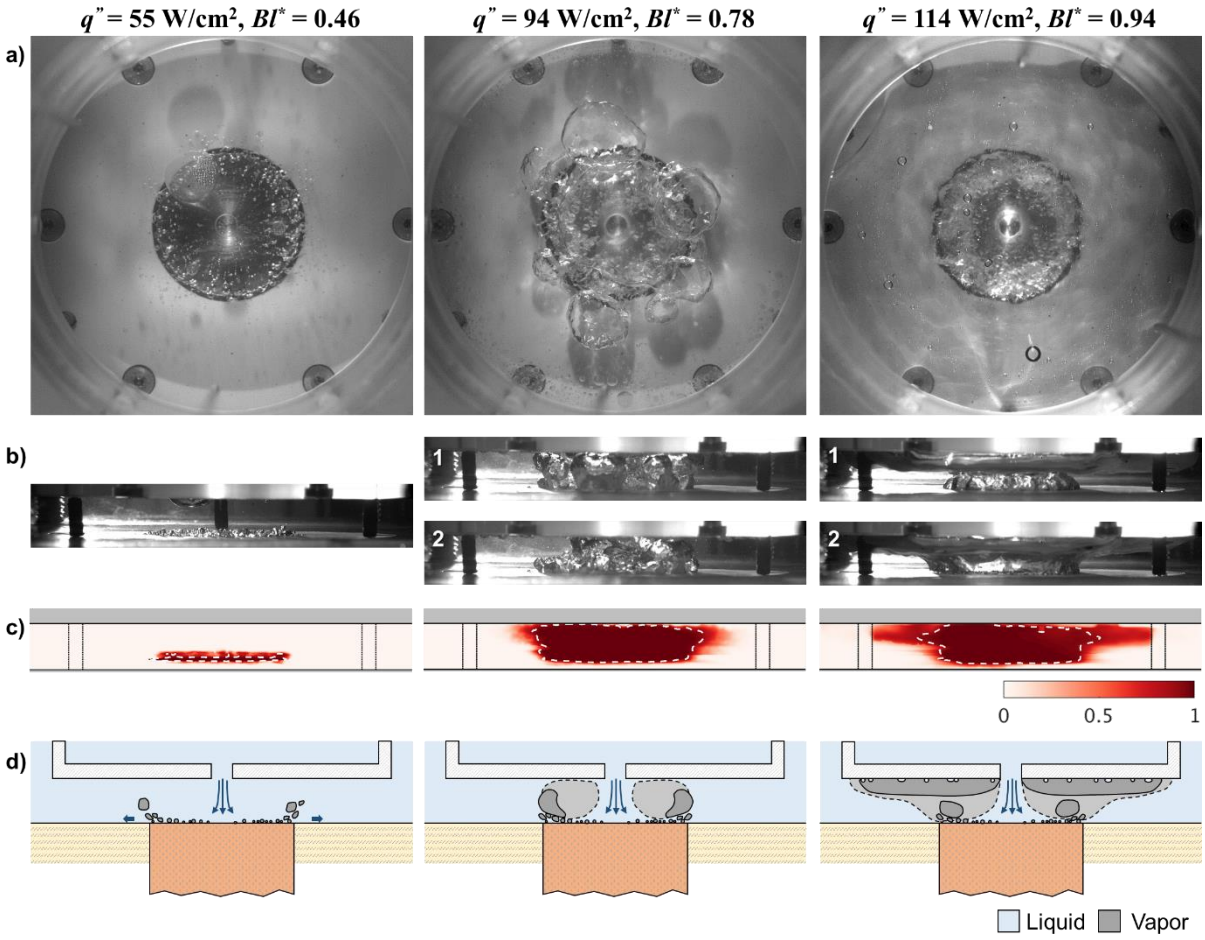

Figure 3. (a) Top-view and (b) side-view observations along with (c) maps of the time-averaged vapor presence from processing of the side-view images of the confinement gap and (d) sketches of the flow morphology during two-phase jet impingement under subcooled exit flow conditions. In (c), a darker shade of red indicates that the vapor is present a higher percentage of the time and the dashed white contour line corresponds to a location where vapor is present 90% of the time. State 1 and state 2, as labelled in the side-view images, are respectively drawn in dark and light gray in the flow morphology sketches. Videos of the top- and side-view visualizations are available in the Appendix.

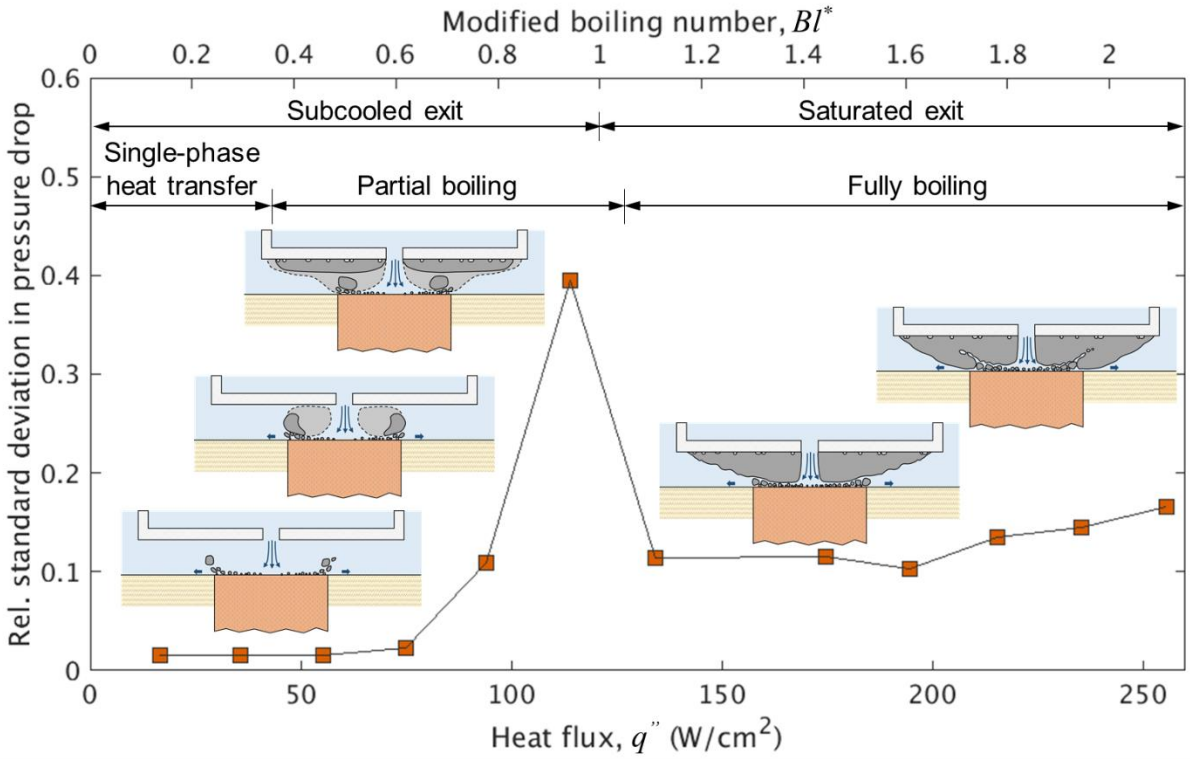

Figure 4. Relative standard deviation in pressure drop between the inlet plenum and downstream of the confinement gap as a function of heat flux. Sketches of flow morphology are included.

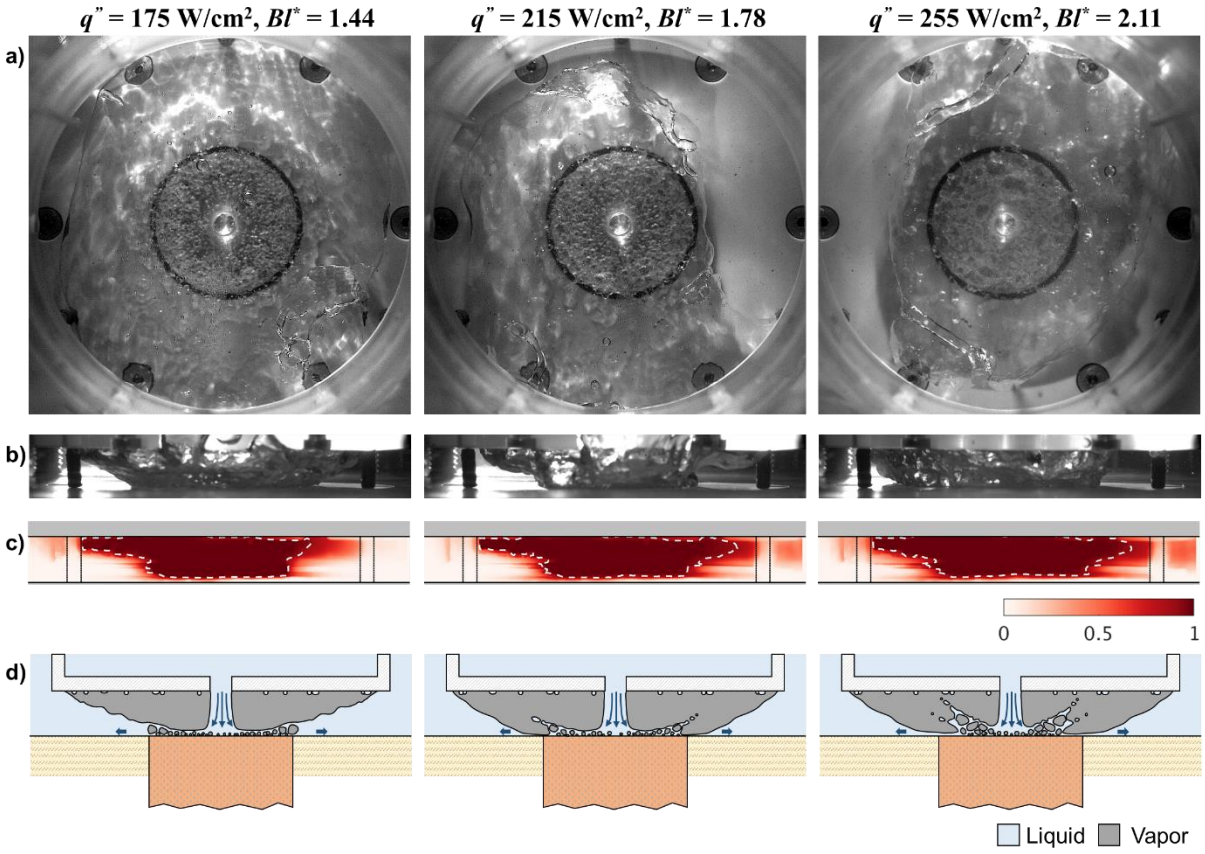

Figure 5. (a) Top-view and (b) side-view observations along with (c) maps of the time-averaged vapor presence from processing of the side-view images of the confinement gap and (d) sketches of the flow morphology during two-phase jet impingement under saturated exit flow conditions. In (c), a darker shade of red indicates that the vapor is present a higher percentage of the time and the dashed white contour line corresponds to a location where vapor is present 90% of the time. Videos of the top- and side-view visualizations are available in the Appendix.

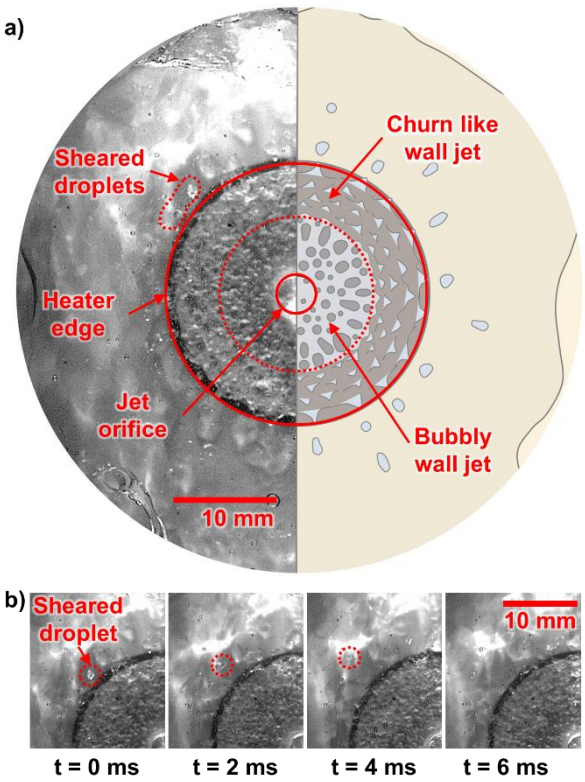

Figure 6. Flow morphology details at q'' = 215 W/cm^2 (Bl^* =1.78) with (a) an annotated top-view image and schematic illustration indicating regimes in the fluid wall jet and (b) time-sequence image frames showing a sheared droplet traveling across the vapor structure and merging with the liquid-vapor interface.